A 3D computational method for determination of pores per inch (PPI) of porous structures

Farshid Jamshidi [a,b,*], Willfried Kunz [a,b], Patrick Altschuh [a,b], Tianyu Lu [b], Matthieu Laqua [b], Anastasia August [a,b], Frank Löffler [c,1], Michael Selzer [a,b], Britta Nestler [a,b]

[a] Institute of Digital Materials Science, Karlsruhe University of Applied Sciences, Moltkestraße 30, 76133 Karlsruhe, Germany
[b] Institute for Applied Materials - Microstructure Modelling and Simulation, Karlsruhe Institute of Technology (KIT), Straße am Forum 7, 76131 Karlsruhe, Germany
[c] Institute for Applied Materials - Ceramic Materials and Technologies, Karlsruhe Institute of Technology (KIT), Kaiserstraße 12, 76131 Karlsruhe, Germany

ARTICLE INFO

Keywords:
Porous materials
Pores per inch (PPI)
Metal foams
Watershed algorithm

ABSTRACT

Due to their special and unique morphology, porous materials have distinctive properties that make them interesting in several sciences and industries. In industrial applications, a popular parameter to characterize the structure of porous materials is the number of pores per inch (PPI). In this work, we implement a computational algorithm in three-dimensional space to determine the PPI number of a porous structure. The algorithm is composed of different steps: segmentation of pore space using a marker-based watershed algorithm, counting the number of pores and eventually calculating the PPI number. To characterize open-cell porous structures according to their PPI values, we generate three types of them. Firstly, an aligned porous structure with a known number of pores is synthetically generated. Excellent agreement between computational results and known values validates our PPI determination algorithm. Secondly, synthetic isotropic/anisotropic porous structures based on Voronoi tessellation (VT) are studied. Finally, we apply the algorithm to the digital twins of real metal foams. The validated proposed approach with reproducible results serves as a unique standard tool to determine the PPI value, and we discuss that it is more precise than conventional two-dimensional methods that are widely used in industry.

1. Introduction

A cellular material such as a foam consists of a solid matrix (liga ment) and void spaces (pores). In addition to the substance of a foam, its morphology, i.e., the shape of pores, the type of pores (closed or open), and their connectivity as well as their spatial distribution in fluence the material properties considerably. Therefore, knowing more about the morphology of foams can lead to the desired properties in a variety of applications such as lightweight construction, sound absorption, mechanical insulation, and heat transfer systems [1 6]. For this purpose, foams need to be classified/characterized, such as the classification conducted in [7]. One of the most commonly used parameters to characterize open cell foams, namely number of pores per inch (PPI) [8] is studied in this paper. PPI is popular in indus trial applications and we introduce computer aided evaluation of this parameter.

The PPI number is frequently used to describe the geometry of open cell solid porous structures and to classify concrete foam samples. This parameter is a favorite manufacturers' specification for cellular solids. But what does the measured PPI really mean? ERG Aerospace Corporation [9] writes: "PPI This is the number of pores per inch of foam". In [10] the PPI number is mentioned as "nominal cell size" but not further defined. In [11] the authors refer to the pore density of 10 and 20 PPI but do not describe how to determine this value and do not provide a reliable definition. Further works on open cell metal foams as [12 16] do not mention PPI at all.

Nevertheless, various PPI measurement methods have been ap plied to characterize foams over the past decades. The number of pores and pore size have been conventionally calculated using optical techniques. Manual measurements have been conducted based on the linear intercept method by drawing random lines on two dimensional

* Corresponding author at: Institute of Digital Materials Science, Karlsruhe University of Applied Sciences, Moltkestraße 30, 76133 Karlsruhe, Germany.
E-mail addresses: farshid.jamshidi@h-ka.de, farshid.jamshidi@kit.edu (F. Jamshidi), willfried.kunz@h-ka.de (W. Kunz), patrick.altschuh@partner.kit.edu (P. Altschuh), tianyu.lu@student.kit.edu (T. Lu), matthieu@laqua.de (M. Laqua), anastasia.august2@kit.edu (A. August), frank.loeffler@kit.edu (F. Löffler), michael.selzer@kit.edu (M. Selzer), britta.nestler@kit.edu (B. Nestler).
[1] Present address: Evonik Operations GmbH, Rodenbacher Chaussee 4, 63457, Hanau, Germany.

(2D) images [17 19]. However, varying the number and location of measurement lines results in different PPI numbers for a single porous medium. One may think that increasing the number of measurement lines can reduce this difference. But by doing so, the workload of man ual measurements becomes heavier and subjective influences cannot be avoided. Even under this circumstance, the inner pores are still not recognizable in a 2D image. To tackle this problem, several three dimensional (3D) imaging approaches and different image processing methods have been introduced in [8,20 24].

Although different techniques of measuring PPI have been employed during the last decades, their results deviate, sometimes significantly, from each other [17]. This happens because counting the number of pores along a straight line with the length of one inch is not so easy as it may sound. The challenges are to answer the following questions precisely and eliminate possible uncertainties: What is a pore, and how should we define the boundary between two interconnected pores (segmentation of pore space)? How are the measurement lines defined? In other words, what are the positions and directions of the measurement line(s)? Does the method work in 2D/3D space? Does the method work for structures with uniform/non uniform pores? Does the method work for structures with stretching of pores, i.e., anisotropic porous media? In this work, we present a solution to overcome these challenges using computational algorithms.

The provided PPI determination algorithm in this work is based on the master's thesis of the fourth author [25]. A similar approach was also used in [8,21]. The remainder of this paper is organized as follows. In Section 2, we introduce the structures together with their generation methods and describe the computational algorithms. Furthermore, we present the results of our study in Section 3. Finally, we summarize the main conclusions of this work in Section 4.

2. Materials and methods

2.1. Generation of porous materials

The aim of the present work is to use the PPI number to characterize open cellular materials such as the structures depicted in Fig. 1. To reach this target, firstly, we generate different types of open cell porous structures and then derive their PPI values. The first synthetically generated structure (Fig. 1a) is an aligned porous structure whose number of pores is known. In other words, we know the PPI value of this structure and expect the same value from the PPI determina tion algorithm represented in Section 2.2.2 in order to validate the algorithm.

The second type of porous structure in this study is synthetically generated based on Voronoi tessellation (VT) (Fig. 1b). Finally, we evaluated the PPI number of real metal foams as the third type of porous medium in this paper. For this purpose, we use two specimens studied in [26], reconstruct them by computed tomography (CT) scan and image processing and subsequently apply the PPI determination algorithm on the gained digital twins (Fig. 1c).

2.1.1. An aligned porous structure

In order to ensure the reliability of the PPI determination algorithm (Section 2.2.2), a structure is required with a precisely known PPI value, i.e., the number of pores. To synthetically generate such a structure, we use the data shown in Table 1. The x, y, and z are three Cartesian axes along which pores are placed. In this table, the number of pores in the x direction is 30, which includes 29 spherical pores as well as two half spherical pores on the domain boundaries. The same interpretation applies to the other two directions. The radius of each pore is 15 cells. The rest of the domain is filled with a solid matrix that results in a structure with highly ordered pores, illustrated in Fig. 1a.

2.1.2. VT based porous structures

The long term goal is to find PPI values of different complex porous structures. One method to synthetically generate such structures is

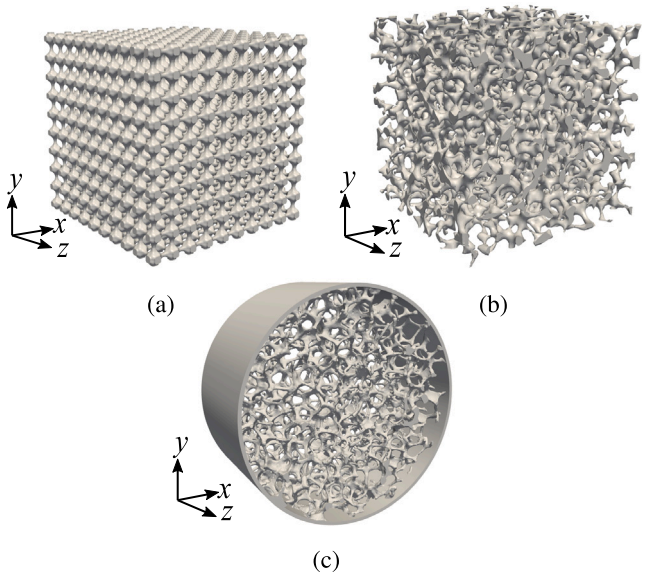

Fig. 1. The 3D representation of porous structures. (a) An aligned open-cell porous structure. (b) A Voronoi tessellation-based porous medium. (c) A digital twin of a real metal foam.

Table 1
The aligned porous structure.

Direction	Domain size (cells)	Number of pores (-)
x	842	30
y	982	35
z	1122	40

based on Voronoi tessellation (VT), which is implemented in our in house software PACE3D [27]. For a more detailed description of the generation process, the reader is referred to [28] and here, we explain it briefly. The process can be divided into the two following major steps:

(I) **Construction of Voronoi diagram:** Initially, some points, which we hereinafter refer to as Voronoi points, are pseudo randomly distributed in the 3D domain. To state it more precisely, it is possible to utilize the same seed to reproduce the same distribution. The number of Voronoi points is predefined. Together with their neighbor cells (voxels), Voronoi points build Voronoi regions under the circumstance that each voxel in the region is assigned to the Voronoi point to which it has the smallest Euclidean distance compared to the distances of this voxel to any other Voronoi point.

(II) **Generating the structure (solid matrix):** By inserting solid spheres on the boundary of at least three Voronoi regions, the solid matrix is generated. Since we specify the volume of pore space in a domain, i.e., the porosity in this work, the ligament radius is adjusted according to the given porosity.

A special form of VT is centroidal Voronoi tessellation (CVT) where each Voronoi point is the center of mass of the corresponding Voronoi region. The CVT used in this work is based on the Lloyd algorithm, which was developed in the late 1960s at Bell Laboratories by S. Lloyd and was later officially published in [29]. Based on the CVT and VT, we generate complex porous structures in this paper using the data shown in Table 2 and PACE3D. Furthermore, geometrical anisotropy can be produced in one or more directions by using anisotropy factors e_x, e_y, and e_z in the x , y , and z directions, respectively. In this work, we use anisotropy factors $0.5 \leq e \leq 1$. As in [30] explained, $e_x = 0.5$ means that firstly, the Voronoi points are placed in the half of the domain in the x direction, secondly, the Voronoi regions are created,

Table 2
The VT-based porous structures.

Domain size (cells)	Generation algorithm	Number of Voronoi points (-)	Porosity (%)	Stretching factor (-)
200 × 200 × 200	CVT	2000, 3000, 4000, 5000	30, 40, 50, 60, 70, 80, 90	1.0
200 × 200 × 200	VT & stretching	4000	90	0.5, 0.6, 0.7, 0.8, 0.9, 1.0

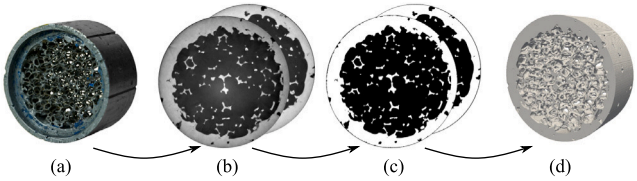

Fig. 2. (a) A real open-cell metal foam sample (10 PPI [26]). (b) Raw CT images. (c) Binarized images. (d) The 3D representation of the digital twin of (a).

and finally, the regions are stretched to fill the whole domain. With e_x less than unity, the porous structure is stretched in the x direction. Therefore, the anisotropy factor can be labeled as the stretching factor. To put it another way, the stretching factor $e_x = 0.5$ means that radii of pores in the x direction are around twice as those of the y and z directions. Nonetheless, $e_{x,y,z} = 1$ corresponds to no stretching and generates isotropic porous structures. The pores are equally sized in any spatial direction.

2.1.3. Real metal foams

The company provided PPI number of two real open cell aluminum alloy foams ($AlSi_7Mg$) studied in [26] are 10 and 30. Here, for com putational study of the two specimens and evaluation of their PPI numbers, we need to precisely reconstruct the structures and generate digital twins of the foams. To achieve this target, we perform computed tomography (CT) scan and image processing and subsequently generate structures (see Fig. 2).

CT scan is an imaging procedure to obtain the (inner) spatial distribution of pores/ligaments. For more details, the reader is referred to [31]. The two real metal foams are CT scanned using a 3D X ray microscope Xradia 520 Versa (Carl Zeiss AG) at the Institute for Applied Materials Ceramic Materials and Technologies at the Karlsruhe Insti tute of Technology. We set the voltage to 80 V and the X ray currents to 87 and 88 A for 10 and 30 PPI specimens, respectively. The size of the images of the 10 PPI specimen is 1004 × 1024 × 1018 voxels or 46.524 × 47.451 × 47.172 mm^3. The images of the 30 PPI specimen consist of the same number of voxels with a different size of 48.749 × 49.720 × 49.428 mm^3. Therefore, the resolution of the images of 10 and 30 PPI specimens are 46.338 and 48.554 μm per pixel in all directions, respectively.

As can be seen in Fig. 2a, the foam does not exist in the entire length of the specimen and subsequently does not appear on all CT images. Thus, only 400 images from 1018 CT images are taken for the next steps. As illustrated in Fig. 2b, the interface between pores and the solid matrix in the CT images is diffuse. By choosing appropriate image processing techniques, the CT images can be converted to a stack of binary images, which only consists of pores and the solid matrix, i.e., the interface between them is sharp. To do so, an open source software, namely Fiji-ImageJ [32] is employed. Using this software, the outer cylindrical shroud is removed, and a suitable threshold for binarization is chosen (Fig. 2c) in such a way that the proportion of pore space in the images is close enough to reality. In other words, the porosity is the criterion for comparison of reconstructed structures with real metal foams. Using PACE3D, the 3D structure is generated based on the image stack (Fig. 2d). As Table 3 shows, the porosities of the reconstructed structures (3D model) are close to those of real metal foams (experimental porosity), which are experimentally derived using gravimetric techniques [26].

Table 3
Validation of porosity.

PPI	Experimental porosity (%)	Porosity of the 3D model (%)
10	88.44 [26]	88.39
30	90.99 [26]	90.83

2.2. Computational algorithms

Building the solid matrix and pore space synthetically gives us the opportunity to determine the PPI number using suitable computational algorithms. To ensure an accurate determination, the pore space must first be segmented into defined pores. For this purpose, the subnetwork of the oversegmented watershed (SNOW) algorithm is implemented in the framework PACE3D. The SNOW algorithm developed by Gostick et al. [33] is based on a marker based watershed segmentation. The next step of this work is to analyze the segmented pore space in order to determine the PPI number in all three spatial directions in the Cartesian coordinate system.

2.2.1. SNOW algorithm

For better understanding of the SNOW algorithm, we briefly de scribe it, and for a deeper insight, we refer the reader to [33]. Because the only difference between the binary image (2D) and the binary image stack (3D) is that the former contains pixels and the latter consists of voxels, it is sufficient that we explain the SNOW algorithm only in 2D in the following five conceptual steps:

I. Preparation of a smoothed Euclidean distance field (SEDF)

Each pixel in the binary image (Fig. 3a) represents either the structure or pore space. By defining a signed distance function, it is possible to generate an Euclidean Distance Field (EDF) of the pore space (Fig. 3b) based on the algorithm of Saito et al. [34]. Moreover, the EDF is smoothed using a Gaussian filter with a variance of $\sigma = 0.35$ [33] to remove spurious peaks, which are misidentified in the distance field.

II. Identification of local maxima in the SEDF

The second step involves the determination of local maxima in the SEDF. For this purpose, the grayscale dilation of the SEDF is calculated using a circular structural element with a radius of five pixels. Then the SEDF is compared pixel by pixel with the grayscale dilation. Pixel pairs that have the same value are stored in a new binary image as local maxima, as shown in red color in Fig. 3c. It is worth mentioning that Gostick et al. [33] conducted numerous tests to find a standard value for the radius of five pixels.

III. Elimination of markers on saddles and plateaus

Now the initial set of local maxima is available, as depicted in Fig. 3c. In the case of parallel ligaments, if neighbor cells in the pore space have an identical distance to the ligaments, then the local maximum does not appear in only one pixel as expected. There are two types of such “erroneous” detected local maxima that are labeled as plateaus (P) and saddles (S), which lead to oversegmentation and need to be filtered. After filtering, only one pixel of a plateau remains, whereas all saddle markers are deleted [33], as shown in Fig. 3d.

IV. Combining nearby maxima

If the Euclidean distance between the markers of a marker pair is smaller than their distances to the structure surface, the marker with the shorter distance is removed. If both markers have the same distance,

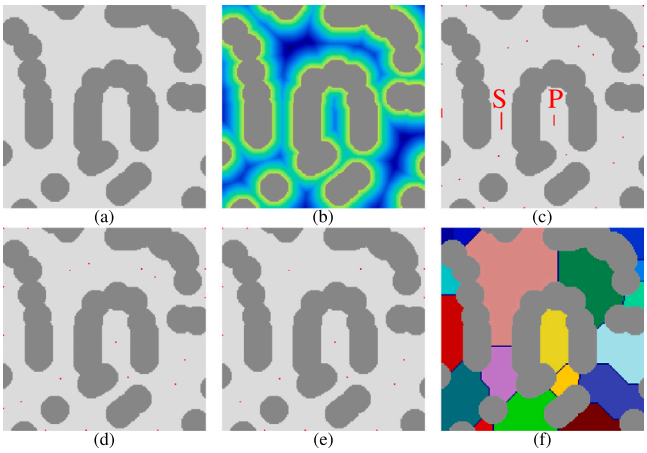

Fig. 3. The schematic illustration of the SNOW algorithm. (a) The initial (2D) binary image with the dark gray structure. (b) The resulting SEDF of the pore space. (c) Identification of local maxima in the SEDF including saddles (S) and plateaus (P). (d) Elimination of markers on saddles and plateaus. (e) Filtering of local maxima in the SEDF. (f) Performing the marker-based watershed segmentation based on the previously identified local maxima.

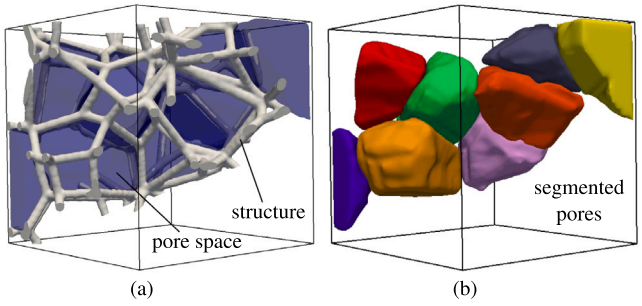

Fig. 4. The 3D representation of marker-based watershed segmentation. (a) The initial binary structure, where the gray color represents the solid structure and the blue color shows the pore space. (b) The resulting segmentation of the pore space.

then one of the two is removed. This reduces all accumulations of markers that were not removed or reduced by the previous steps to one marker as shown in Fig. 3e.

V. Performing marker-based watershed algorithm

The set of filtered markers together with the EDF is passed to a marker based watershed algorithm that performs the segmentation of the pore space. The algorithm of Pierre Soille [35], which is included in the ITK library [36], is used. The result of the segmentation is a map in which each pixel is uniquely associated with a segment via a corresponding marker (Fig. 3f). By using this algorithm, the number of markers determines the number of segments in the resulting figure. The result of an entire segmentation in 3D is exemplary represented in Fig. 4.

2.2.2. PPI determination

By using the previously described SNOW algorithm, the pore space has been segmented, where each voxel (3D) has a defined pore identifi cation number. Now, we explain the computational PPI determination in the following steps:

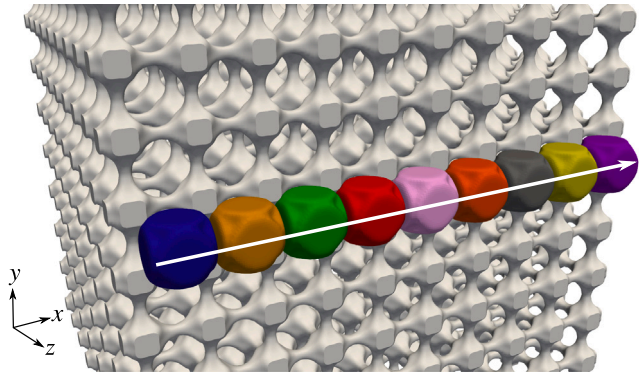

Fig. 5. The 3D representation of a measurement line and its corresponding pores. The colored parts represent the pores, the gray color shows the solid structure, and the white arrow displays one measurement line in the x-direction.

I. Definition of the measurement lines

To calculate the PPI number, we draw some lines through the domain and count the number of entire pores they passed through. We label these lines as measurement lines hereinafter. To give a clear pic ture of how we define these lines, we use the concept of computational resolution in the Cartesian coordinate system. Thus, the xy , xz and yz planes contain the defined numbers of cells. From each cell on a plane, a measurement line is drawn perpendicular to the corresponding plane. For instance, measurement lines are drawn from the xy plane parallel to the z axis.

The number and directions of measurement lines are defined. First, the start and end of each line is registered. On a measurement line, we count only the pores that are entirely located in the domain and not on the boundaries. The reason for ignoring boundary pores is that we have no information about the rest of their shapes outside the domain. Therefore, the length of measurement lines in each direction is not identical and their start and end points must be adjusted, as implemented in Functions 1 and 2 of the algorithm (see Appendix).

II. The number of pores

Now, we know where the measurement lines begin and where they end. The next step is to count the number of pores alongside the measurement lines, which is accomplished using Function 3 (see Ap pendix). We display a measurement line together with its corresponding pores in Fig. 5.

III. Calculation of the average PPI (PP100C) number

In computational calculation, it is more efficient to work with dimensionless parameters. Therefore, we count the number of pores per all cells along a measurement line, calculate how many pores exist in 100 cells on average, and finally save this new parameter as PP100C. Then, by knowing the physical length of each cell, it is possible to convert PP100C to PPI. For calculation of PP100C, we only consider the measurement lines that pass through at least one pore and label them as valid lines. The measurement lines that pass through only the solid matrix are not considered for further calculation. As indicated before, the measurement lines are parallel to the axes of the Cartesian coordinate system. Thus, we add the PP100C values of all "valid" measurement lines in x direction and divide the summation by the number of these lines. This results in the mean value of PP100C in x direction, namely $PP100C_x$ (see Functions 4 and 5 in Appendix). Fig. 6 depicts how our algorithm computes $PP100C_x$. By analogy, we calculate the value of $PP100C_y$ and $PP100C_z$. The arithmetic average of these values is PP100C.

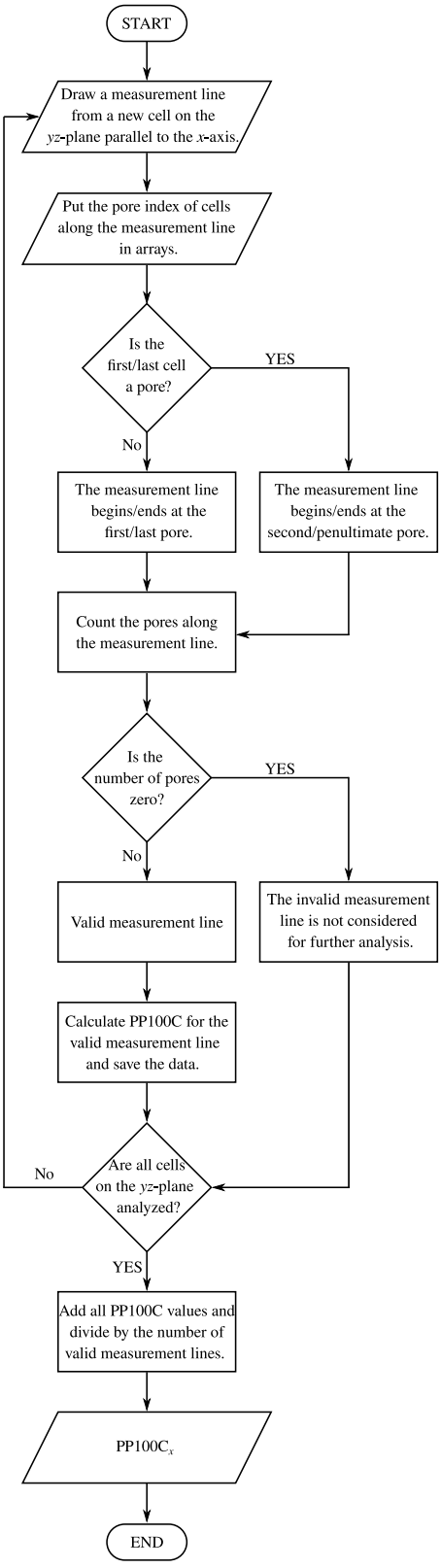

Fig. 6. The flowchart to compute PP100C$_x$.

3. Results and analysis

3.1. Validation

As explained in Section 2.1.1, we build a uniform pore space to validate the PPI determination algorithm. From Table 1, we expect PP100C = 3.56 in all three directions. From the determination algorithm, we obtain the PPI value of 3.575, 3.576 and 3.581 for the x, y, and z directions, respectively; these correspond to an error of less than 0.5 %. Thus, as expected values and computed results are very close to each other, we can conclude that the algorithm is reliable and our validation is accomplished.

3.2. PP100C of VT based porous structures

As Table 2 shows, we generate different porous structures based on Voronoi tessellation and analyze them regarding their PP100C values.

CVT based porous structures without stretching

In Fig. 7, we show only the average PP100C using the PPI determination algorithm as we do not observe a significant difference among the values in x, y and z directions. As expected, for CVT based structures (Fig. 7a), PP100C increases with the number of Voronoi points. The reason is that the number of Voronoi points correlates with the number of pores for the same domain size [37], and with more Voronoi points, more pores are detected along measurement lines. In addition, PP100C increases with porosity for a constant number of Voronoi points.

Because PP100C (or PPI) is a one dimensional parameter and Voronoi points build 3D Voronoi regions, we expect that the third root of the number of Voronoi Points is proportional to PP100C. To examine this, we calculate the arithmetic mean of the average PP100C values for all porosities with a defined number of Voronoi points and plot it dimensionlessly against the third root of the number of Voronoi points in Fig. 7b. As can be seen, the slope of the curve is constant, which completely fulfills our expectation. However, averaging data leads to the loss of details, which is not the aim of this study.

Distribution and anisotropy of pores affect mechanical properties of porous materials as well as fluid flow through them. Therefore, studying the relationship between PPI and stretching of pores is beneficial for characterization of porous structures. As mentioned in Section 2.1.2, we generate VT based porous structures with the stretching factors, $e_{x,y,z}$ from 0.5 to 1.0 in order to study the effect of stretching on PP100C.

VT based porous structures with stretching in one direction

Fig. 8 shows PP100C in three spatial directions for structures with stretching only in the x direction. It is important to mention that porosities of two structures with different stretching factors (e_x) in spite of the same Voronoi points in the same domain size are not identical. To generate structures with the equal porosity of 90% (see Table 2) and different e_x, slight changes in pores radii in the y and z directions are inevitable. This impacts on PP100C in the two latter directions.

As stated previously, no stretching factor refers to the unity values ($e_x = e_y = e_z = 1$). Thus, all the PP100C values by $e_x = 1$ are roughly the same and around 8.67. If we reduce the value of e_x, then the pores are stretched more in the x direction that results in a gradual decrease of PP100C in this direction. For instance, by $e_x = 0.5$, PP100C$_x$ is near 6.52. In contrast, PP100C$_y$ and PP100C$_z$ increase slightly by the decline in e_x. Their curves demonstrate the same trend and approximately the same values, since there is no stretching in these directions ($e_y = e_z = 1$) and the changes are just due to the variation of e_x. The values of PP100C$_y$ and PP100C$_z$ are approximately 9.8 by $e_x = 0.5$. It should be mentioned that each point in Figs. 7a and 8 represents the mean value of five evaluated structures with different seeds. Since the relative standard deviation is always less than 4.75 %, the deviations are not shown in these diagrams for the sake of clarity.

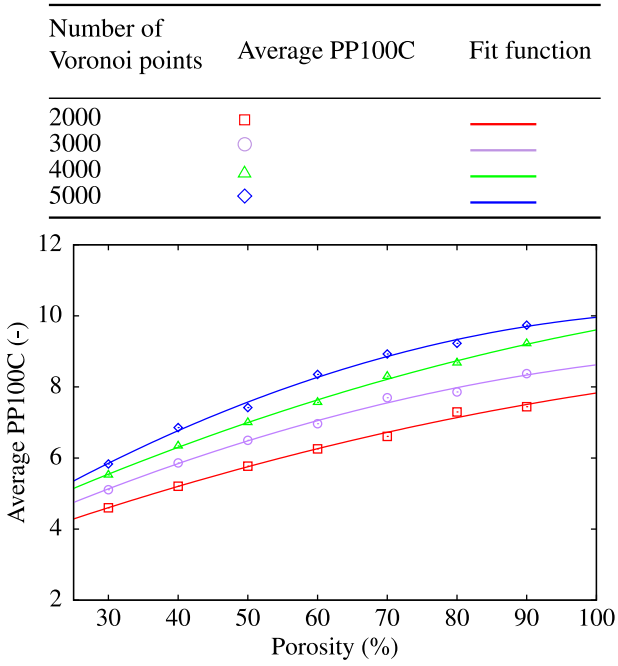

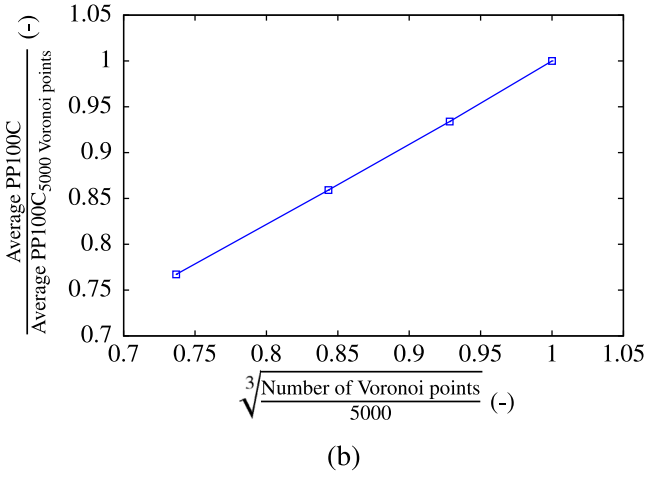

Fig. 7. (a) The average number of pores per 100 cells (PP100C) for CVT-based structures where the number of Voronoi points and porosity vary. Each point represents data from five structures with different seeds. (b) The correlation between average PP100C and the number of Voronoi points.

VT based porous structures with stretching in two directions

We generate structures with stretching in both x and y directions, and we show their PP100C values in Fig. 9. If the stretching factors are equal ($e_x = e_y$), the PP100C values in both directions are approximately the same. In other words, the fitting curves of $PP100C_x$ and $PP100C_y$ intersect around the points where the stretching factors are identical in both directions. Moreover, for all e_x values, $PP100C_y$ raises as e_y increases, while $PP100C_x$ and $PP100C_z$ gradually decrease. In Fig. 9f, the stretching factor in the x direction is 1.0 (i.e., no stretching) and $PP100C_x$ and $PP100C_z$ are very close to each other, as expected from the previous investigation. From this analysis, we conclude that more stretching in a certain direction results in a smaller PP100C value in that specific direction. All shown points in Fig. 9 represent the mean value of three structures with different seeds where the relative standard deviation of each point is always smaller than 4.65 %.

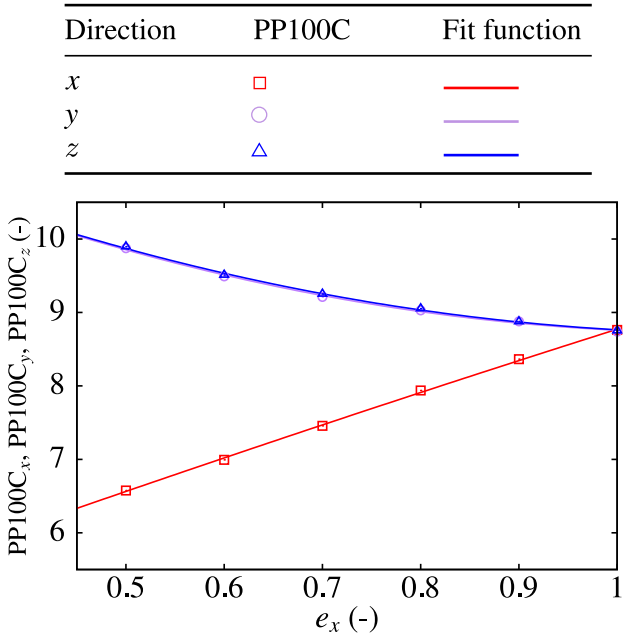

Fig. 8. The number of pores per 100 cells (PP100C) for structures with stretching in the x-direction. Each point represents data from five structures with different seeds.

Comparison of VT based porous structures without and with stretching

To demonstrate how stretching affects the PP100C values in all directions, we plot all the PP100C values for the stretching factors 0.5, 0.7 and 1.0 Fig. 10. It can be seen that stretching the pores in a direction reduces the value of the PP100C in that direction. Also, more intense stretching leads to smaller PP100C values. Moreover, as it is illustrated in Fig. 10a and b, sole stretching in one direction has less influence on PP100C compared to that in two directions. We arrive to the same conclusion by observing Fig. 10c, where smaller stretching factors (more stretching) in both directions lead to smaller PP100C values in the corresponding directions.

In addition, $PP100C_z$ is indirectly influenced by stretching in x and y directions. For instance, with stretching factors of 0.5, $PP100C_z$ is the largest among the depicted values. The smaller the stretching factor in a certain direction is, the larger the PP100C values in the remaining directions become. However, for the structures with the same porosity and the same number of Voronoi points in the same domain size, the average PP100C does not significantly vary with stretching the pores.

In summary, if stretching is only in the x direction, $PP100C_x$ is much smaller than $PP100C_y$ and $PP100C_z$ and is influenced deeply by the stretching factor. When stretching occurs in two directions (i.e. x and y), $PP100C_x$ reduces not so much as when stretching is only in one direction.

3.3. PPI of real metal foams

By using our determination algorithm, we are able to find the PP100C values of the digital twins of the real metal foams. By using the values of image resolution form Section 2.1.3, we convert computed PP100C to the PPI values and compare them with the Company provided PPI values from [26] in Table 4. As can be seen, the PPI values are smaller than those given by the manufacturer. In the case of the sample with the company provided PPI value of 10, the average PPI value calculated by the presented algorithm differs by 10.01 %. Additionally, based on the results of Section 3.2, a structural anisotropy can be observed. Thereby, the PPI values in the x and y directions do not differ greatly, whereas in comparison the PPI value in the z direction shows a smaller value. This indicates that the sample has

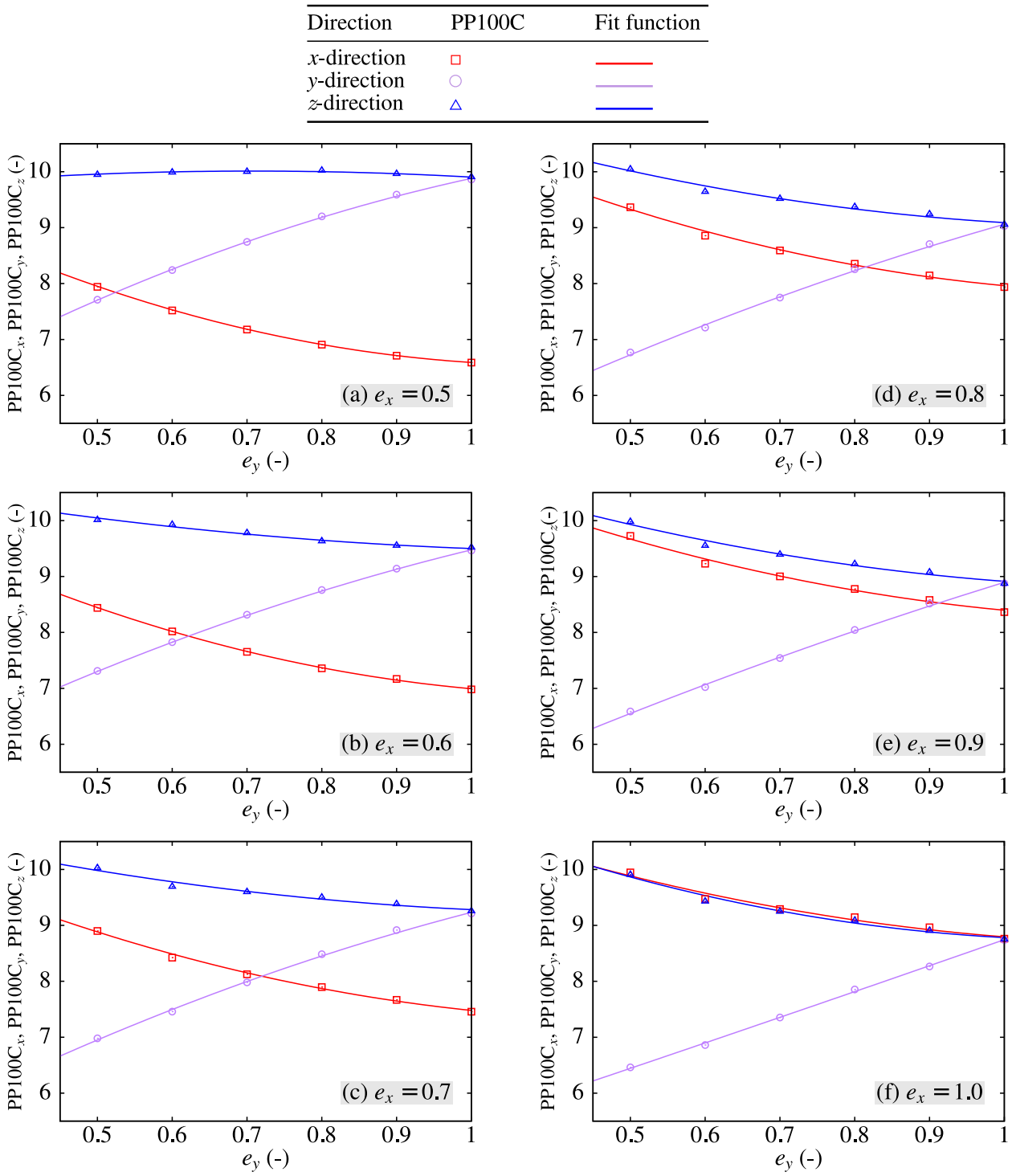

Fig. 9. PP100C for structures with stretching in the x and y-directions where for each plot, the stretching factor in the x-direction is constant and displayed in the legend. Each point represents data from three structures with different seeds.

a structural stretch along the z axis. In the case of the sample with the company provided PPI value of 30, the differences are greater, specially in z direction. A possible reason might be the short length of the real metal foam in this direction ($\approx$2 cm) that is not representative. Another reason can be the anisotropy of the structures observed by looking at the xy cross section. The pores are indeed stretched along the z direction, which results in a smaller PPI number in this direction.

4. Discussion and conclusion

When we observe a porous medium and aim to count its pores, we probably see a structure such as in Fig. 11a, which is generated synthetically based on CVT. Our eyes can only detect front layers of the pore space. For better visualization, a turquoise plane is added behind the front layers. We see the skeleton as the borders of the pore space. In

Table 4
Comparison between company-provided and computed PPI values.

Company-provided PPI (-)	Computed PPI (-) in different directions and on average			
	PPI_x	PPI_y	PPI_z	Average PPI
10	9.4604	9.7989	7.7217	**8.99**
30	14.570	13.993	11.555	**13.37**

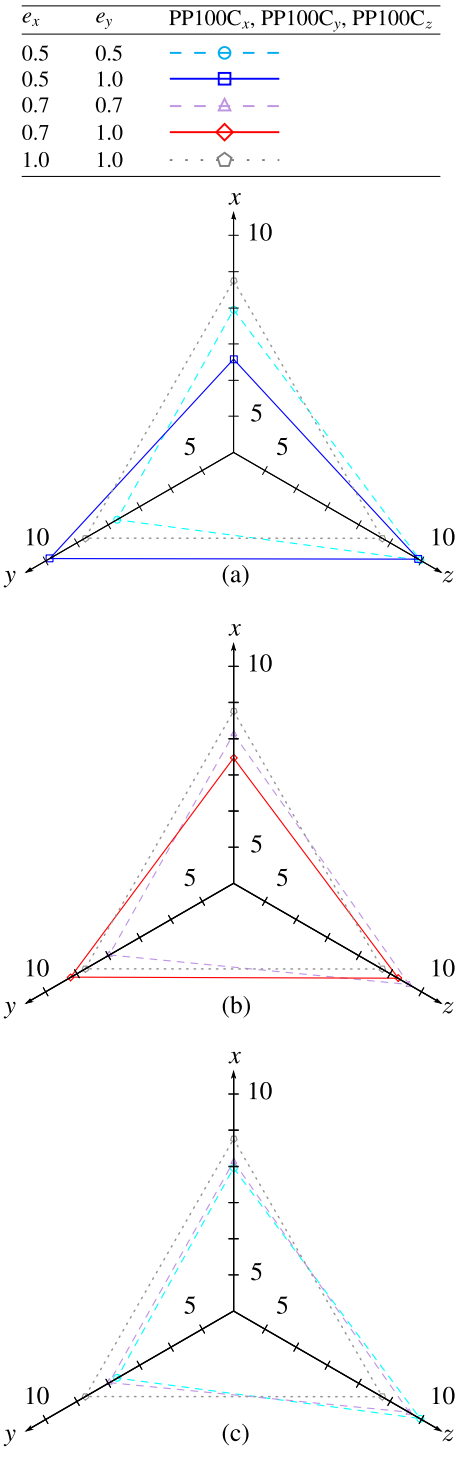

Fig. 10. PP100C of structures without stretching (gray dotted lines), with stretching in one direction (blue/red solid lines) and with stretching in two directions (cyan/magenta dashed lines). Note that for all structures $e_z = 1$.

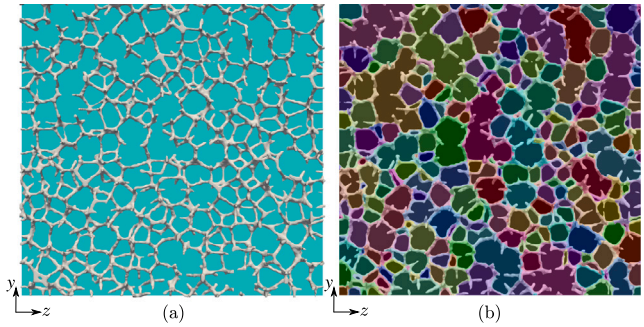

Fig. 11. (a) A synthetically generated porous structure. (b) Segmentation of pore space using a watershed algorithm.

Fig. 11b, each region surrounded by ligaments is illustrated by a color. This is performed by a watershed segmentation [38] implemented in Fiji-ImageJ [32]. We can draw some lines, count the number of regions and eventually calculate the PPI number. But there are a few problems in adopting this approach. First, we do not know that a region that is seen as a single region is comprised of a single or more than one pore. This is because we cannot fully detect the connections amongst different parts of the skeleton that are not visible in the plane of the 2D image. Second, varying the number and position of the measurement lines may change the PPI number significantly [17]. This is because we are solely relying on two instead of three dimensions of the structure. These problems are intrinsic to every 2D evaluation. This was tried to be addressed in [8] where the authors represent a modified 2D model, however, a calibration based on the 3D image processing was also needed.

The first objective of our work was to segment the pore space of porous structures and implement a counting algorithm that can accurately compute the number of pores. By knowing the precise number of pores, it is possible to obtain the accurate value of PPI (pores per inch). This is crucial for real structures where we need to determine the difference between the PPI number of the reconstructed structure and that given by the manufacturer. For further analysis and characterization, many morphological properties of the structure should be taken into account. Therefore, having a model in which individual pores can be accurately distinguished is necessary. The algorithm presented here is the first step in developing such a computer model. Its accuracy is verified using an aligned structure. It can be used in three dimensional geometries, which demonstrates the superiority of a computer calculation over traditional PPI measurements.

Generally, in computer generated or computer reconstructed structures, the pores are distinguished by marker based watershed algorithms and PPI can be computed in three spatial directions. With the counting algorithm, compared to conventional methods, more measurement lines can be placed in the entire volume of the structure, which can eliminate the influence of location on the result and the randomness of manual measurements. In the PPI determination algorithm, the length of the measurement line is adjusted according to the identified pores inside the domain. With outstanding computing capacity, the calculation can be performed over a short period of time and provide more accurate information about porous materials.

Based on the performed PPI investigation of VT based porous structures, the general rules of the variation of PPI are as follows: For the structures with the same porosity, those with higher numbers of Voronoi points (pores) have higher PPI values. When the structures have the same number of Voronoi points, PPI increases with increasing porosity.

Porous structures with stretched pores in targeted directions are also common in industrial production. Therefore, the relationship between PPI and stretching of the pores is noteworthy. The stretching of pores affects the mechanical properties and the permeation of liquids in porous structures as well. In the absence of stretching, the PPI numbers in the three directions are identical. When the pores are stretched in one direction, the PPI number in that direction becomes smaller and increases in the other directions (see Fig. 8). With a higher degree of stretching (in this paper, a smaller stretching factor), the variation of the PPI number in all directions increases. In cases where stretching occurs in two directions, the PPI values in both directions are lower than in the unstretched one and if the degree of stretching is the same in both directions, the PPI is approximately the same (see Fig. 9). When the conditions required to generate the structure do not change, the direction and degree of stretching of the pores do not significantly affect the average PPI number in the entire volume.

We also implement the PPI determination algorithm for real structures. First, the structure is reconstructed from CT images and then PPI values are computed. The results have smaller values than those given by the manufacturer, specially for structures with the larger PPI value.

We use the algorithm to study the effect of pore numbers and porosity on PPI. In the future, the position of the measurement lines can be further improved, for example by not placing measurement lines in the same direction as the axes. Furthermore, comparing the PPI values in three spatial directions with their arithmetic average can demonstrate stretching of pores.

CRediT authorship contribution statement

Farshid Jamshidi: Conceptualization, Methodology, Writing original draft. **Willfried Kunz:** Methodology, Software, Writing review & editing. **Patrick Altschuh:** Conceptualization, Writing review & editing. **Tianyu Lu:** Validation, Investigation, Visualization. **Matthieu Laqua:** Methodology, Software. **Anastasia August:** Writing review & editing. **Frank Löffler:** Resources, Writing review & editing. **Michael Selzer:** Software, Data curation. **Britta Nestler:** Writing review & editing, Supervision, Funding acquisition.

Declaration of competing interest

The authors declare that they have no known competing financial interests or personal relationships that could have appeared to influence the work reported in this paper.

Data availability

The authors do not have permission to share data.

Acknowledgments

This work was supported by Leistungsorientierte Förderung des akademischen Mittelbaus für Forschungsgruppen an HAW, Germany and by the Helmholtz association within the program “Materials Systems Engineering" (MSE). The second author was supported by the German government through the BMBF project Multipore (project ID: 13FH020KX0). The third author thanks the Ministry of Science, Research and the Arts Baden Württemberg (MWK BW), Germany, in the project MoMaF Science Data Center, with funds from the state digitization strategy digital@bw (project number 57).

Appendix. Pseudo-code of the PPI determination algorithm

Function 1: The function to find the beginning of the measurement line: *Line Begin*()
This function determines the beginning of the measurement line whether it be at the first pore or the second pore. If the measurement line meets no pore, the beginning of the measurement line will be the last cell of the structure.

Input :
store[]: the array to store the index of cells
len: the domain in the chosen direction
Output :
find the beginning location of measurement line

```
count ← 0
if store[0] is pore then
    count ← count + 1
end if
for i ← 1 to len − 1 do
    if store[i] is a pore and different from the previous pores then
        count ← count + 1
    end if
    if store[0] is not a pore and count == 1 then
        break
    else if count == 2 then
        break
    end if
end for
if i == len then
    return len − 1                ▷ measurement line meets no pore
else
    return i
end if
```

Function 2: The function to find the end of the measurement line: *Line End*()
This function determines the end of the measurement line whether it be at the last pore or penultimate pore. If the measurement line meets no pore, the end of the measurement line will be the first cell of the structure.

Input :
store[]: the array to store the index of cells
len: the domain in the chosen direction
Output :
find the end location of measurement line

```
count ← 0
if store[len − 1] is pore then
    count ← count + 1
end if
for i ← len − 2 to 0 do
    if store[i] is a pore and different from the previous pores then
        count ← count + 1
    end if
    if store[len − 1] is not a pore and count == 1 then
        break
    else if count == 2 then
        break
    end if
end for
if i == −1 then
    return 0                      ▷ measurement line meets no pore
```

```
    else
        return i
    end if
```

Function 3: The function to count the pores: $PoreNumber()$
After knowing the start and end of the measurement line from Functions 1 and 2, this function gives the number of pores on the measurement line.

Input :
$store[]$: the array to store the index of cells
$begin, end$: the begin and end of the measurement line
$length$: the length of the measurement line
Output :
the number of pores

```
count ← 0
if store[begin] is pore then
    count = count + 1
end if
for i ← begin + 1 to end do
    if store[i] is a new pore then
        count = count + 1
    end if
end for
return count
```

Function 4: The function to calculate the length and get the number of pores: $Get\ Result()$
This function calculates the length of each measurement line and calls the output of the Function 3 to produce the final result in the form PP100C. If the beginning of the measurement line lies after its end, then the line does not encounter any pore and the result is zero.

Input :
$store[]$: the array to store the index of cells
$begin, end$: the begin and end of the measurement line
Output :
PP100C

```
result ← 0
length ← 0
if begin ⩾ end then
    result ← 0
else
    length ← end − begin + 1
    result = PoreNumber() × 100 ÷ length
end if
return result
```

Function 5: The function to calculate the average PP100C in x direction
This function shows how the PPI determination algorithm works in one direction. The "invalid" measurement lines are not counted in the average.

Input :
$x\ max, y\ max, y\ max$: the domain in different directions
Output :
average PP100C in x direction

```
times v ← 0
times np ← 0
sum ← 0
if choose the x direction then
    for dir y ← 0 to y max do
        times p ← 0
        times v ← times v + 1
        for dir z ← 0 to z max do
            times p ← times p + 1
            for dir z ← 0 to z max do
                put the index of cells into array tmp store[]
            end for
            find the begin and end of the measurement line
Line Begin(), Line End()
            get the number of pores in this measurement line result ←
Get Result()
            if result == 0 then
                times np ← times np + 1                ▷ Count the invalid
measurement lines
            end if
            sum ← sum + result
        end for
    end for
    times total ← times v × times p    times np
    average ← sum ÷ times total
    return average
end if
```

References

[1] G.M. Gladysz, K.K. Chawla, Chapter 6 - cellular materials, in: G.M. Gladysz, K.K. Chawla (Eds.), Voids in Materials, Elsevier, Amsterdam, 2015, pp. 103–130.
[2] J. Banhart, Manufacture, characterisation and application of cellular metals and metal foams, Prog. Mater. Sci. 46 (6) (2001) 559–632.
[3] L.J. Gibson, Cellular solids, MRS Bull. 28 (4) (2003) 270–274.
[4] A. August, F. Jamshidi, a.R.H.W. A. Kneer, M. Wirtz, B. Nestler, Development of synthetic open porous structures for improved heat transfer, Int. J. Heat Mass Transf. 159 (2020) 120071.
[5] M. Sahimi, Flow and Transport in Porous Media and Fractured Rock: From Classical Methods To Modern Approaches, John Wiley & Sons, 2011.
[6] X. Yu, Z. Lu, W. Zhai, Enhancing the flow resistance and sound absorption of open-cell metallic foams by creating partially-open windows, Acta Mater. 206 (2021) 116666.
[7] D. Bhate, C.A. Penick, L.A. Ferry, C. Lee, Classification and selection of cellular materials in mechanical design: Engineering and biomimetic approaches, Designs 3 (1) (2019).
[8] J. Ohser, C. Redenbach, A. Moghiseh, The PPI value of open foams and its estimation using image analysis, Int. J. Mater. Res. 105 (7) (2014) 671–678.
[9] ERG, Duocel aluminum foams, 2022, Homepage.
[10] K.S. Jang W., A. Kraynik, On the microstructure of open-cell foams and its effect on elastic properties, Int. J. Solids Struct. 45 (7–8) (2008) 1845–1875.
[11] K.C. Girlich D., K. Hackeschmidt, Bestimmung des konvektiven Wärmeübergangs offenporiger Metallschäume, Konstruktion 1 (2) (2005) 54–58.
[12] G.E. Kopanidis A., A. Theodorakakos, D. Bouris, 3D numerical simulation of flow and conjugate heat transfer through a pore scale model of high porosity open cell metal foam, Int. J. Heat Mass Transfer 53 (11) (2010) 2539–2550.
[13] P.D. Boomsma K., On the effective thermal conductivity of a three-dimensionally structured fluid-saturated metal foam, Int. J. Heat Mass Transfer 44 (4) (2001) 827–836.
[14] H. Wadley, Cellular metals manufacturing, Adv. Eng. Mater. 4 (10) (2002) 726–733.
[15] J. Banhart, Metal foams: production and stability, Adv. Eng. Mater. 8 (9) (2006) 781–794.
[16] C. Redenbach, Modelling foam structures using random tessellations, stereology and image analysis, in: Proc 10th Eur Conf ISS (ECS10), Vol. 4, 2009.
[17] M. Scheffler, P. Colombo, Cellular Ceramics: Structure, Manufacturing, Properties and Applications, John Wiley & Sons, 2006.
[18] T.B. Sweeting, D.A. Norris, L.A. Strom, J.R. Morris, Reticulated ceramics for catalyst support applications, MRS Proc. 368 (1994) 309.
[19] J. Richardson, Y. Peng, D. Remue, Properties of ceramic foam catalyst supports: pressure drop, Appl. Catal. A: Gen. 204 (1) (2000) 19–32.

[20] C. Liu, G. Liu, Characterization of pore structure parameters of foam concrete by 3D reconstruction and image analysis, Constr. Build. Mater. 267 (2021) 120958.
[21] A. Liebscher, C. Redenbach, 3D image analysis and stochastic modelling of open foams, Int. J. Mater. Res. 103 (2) (2012) 155–161.
[22] M. Beer, M. Taušová, R. Rybár, M. Kalavský, A novel economical method of determining the geometric characteristic of the metal foam based on image analysis, Energies 13 (13) (2020).
[23] J. Ohser, K. Schladitz, 3D images of materials structures, 2010.
[24] C.R. Appoloni, C.P. Fernandes, M.D.d.M. Innocentini, Á. Macedo, Ceramic foams porous microstructure characterization by X-ray microtomography, Mater. Res. 7 (2004) 557–564.
[25] T. Lu, Spatial distribution of pores in porous materials [Räumliche Verteilung von Poren in porösen Materialien] (Master's thesis), Karlsruher Institut für Technologie (KIT), 2022.
[26] J. Ettrich, Fluid Flow and Heat Transfer in Cellular Solids, Vol. 39, KIT Scientific Publishing, 2014.
[27] J. Hötzer, A. Reiter, H. Hierl, P. Steinmetz, M. Selzer, B. Nestler, The parallel multi-physics phase-field framework Pace3D, J. Comput. Sci. 26 (2018) 1–12.
[28] P. Altschuh, Y.C. Yabansu, J. Hötzer, M. Selzer, B. Nestler, S.R. Kalidindi, Data science approaches for microstructure quantification and feature identification in porous membranes, J. Membr. Sci. 540 (2017) 88–97.
[29] S. Lloyd, Least squares quantization in PCM, IEEE Trans. Inform. Theory 28 (2) (1982) 129–137.
[30] P. Altschuh, SkalenÜbergreifende Analyse MakroporÖser Membranen Im Kontext Digitaler Zwillinge (Ph.D. thesis), Karlsruher Institut für Technologie (KIT), 2020, p. 372.
[31] T. Bultreys, W. De Boever, V. Cnudde, Imaging and image-based fluid transport modeling at the pore scale in geological materials: A practical introduction to the current state-of-the-art, Earth-Sci. Rev. 155 (2016) 93–128.
[32] J. Schindelin, I. Arganda-Carreras, E. Frise, V. Kaynig, M. Longair, T. Pietzsch, S. Preibisch, C. Rueden, S. Saalfeld, B. Schmid, J.-Y. Tinevez, D.J. White, V. Hartenstein, K. Eliceiri, P. Tomancak, A. Cardona, Fiji: an open-source platform for biological-image analysis, Nature Methods 9 (7) (2012) 676–682.
[33] J.T. Gostick, Versatile and efficient pore network extraction method using marker-based watershed segmentation, Phys. Rev. E 96 (2) (2017) 023307.
[34] T. Saito, J.-I. Toriwaki, New algorithms for euclidean distance transformation of an n-dimensional digitized picture with applications, Pattern Recognit. 27 (11) (1994) 1551–1565.
[35] P. Soille, Morphological Image Analysis: Principles and Applications, Springer Science & Business Media, 2013.
[36] M. McCormick, X. Liu, J. Jomier, C. Marion, L. Ibanez, ITK: enabling reproducible research and open science, Front. Neuroinf. 2014 (8) (2014) 13, 2002.
[37] A. August, B. Nestler, On counting cells in open pore foams, Eng. Res. Express 2 (2) (2020) 025029.
[38] D. Legland, I. Arganda-Carreras, P. Andrey, MorphoLibJ: integrated library and plugins for mathematical morphology with imagej, Bioinformatics 32 (22) (2016) 3532–3534.